Reports on Geodesy and Geoinformatics, 2025, Vol. 120, pp. 31–39

DOI: 10.2478/rgg-2025-0014
Received: 17 February 2025 / Accepted: 4 September 2025
Published online: 19 September 2025

ORIGINAL ARTICLE

Application of GNSS antenna vibration simulator to validation of dynamic displacement detection systems

Radoslaw Baryla [1*]

[1]Department of Geodesy, University of Warmia and Mazury in Olsztyn, Oczapowskiego 2, 10-719, Olsztyn, Poland

[*]radoslaw.baryla@uwm.edu.pl

Abstract

A Global Navigation Satellite System (GNSS) antenna vibration simulator was developed to support the validation of dynamic position sensing systems. Based on a stepper motor mechanism, the device generates controlled reciprocating motion through a connecting rod, offering a simple and user-friendly design. Field experiments were conducted to assess its performance, with motion parameters – displacement, velocity, and acceleration – measured and compared against theoretical sinusoidal models. The simulator was employed to evaluate GNSS+Inertial Measurement Unit (IMU) receivers and associated software designed for detecting and monitoring dynamic displacements. High-frequency GNSS data, collected under real-world conditions at the KGHM Cuprum R&D Centre in Lubin, Poland, were processed to extract antenna position time series and assess simulated motion accuracy. Fourier transform analysis of the displacement signals confirmed the simulator's effectiveness in replicating dynamic motion, demonstrating its suitability for testing GNSS-based displacement monitoring systems.

Key words: vibration simulator, GNSS, low-cost GNSS receiver, IMU

1 Introduction

Exploration of natural resources is an essential element of the global economy and is becoming increasingly challenging. The most abundant natural resources in Poland include hard coal and lignite, copper and silver ores, natural gas, and crude oil (Galos et al., 2010; Szuflicki et al., 2024). Depending on physical properties of those natural resources and their form and the depth of their deposits, a range of mining technologies are used, including: surface, underground, borehole (drilling), and undersea. Open-dip and deep mining necessitate the removal of groundwater, which would otherwise pose hazards to exploitation of deposits. However, this process leads to the formation of extensive cones of depression, resulting in terrain transformation commonly referred to as land deformation.

The extraction of natural resources interferes with the structure of the rock mass, which becomes distorted by the voids left after removing parts of the deposits, thereby causing tensions. Exceeding the stress threshold values leads to localised destruction of the rock mass, including cracks, fissures, and displacements. At the same time, the released energy causes seismic shocks, examples of which are detailed in the literature (Duff et al., 2011; Sainoki et al., 2020; Shirani Faradonbeh et al., 2022). Seismic tremors in the form of longitudinal and transverse waves travel toward the Earth's surface, resulting in earthquakes, whose strength in each site depends on the amount of energy released and the distance from the epicentre. In Poland, tremors are sensed in areas affected by hard coal and lignite mines and in the Legnica-Głogów Copper Belt. Tremors and land relief deformations in these areas can lead to significant damage both to the land surface (cracks in buildings, sinkholes) and underground (cracks in ceilings, landslides, collapses), causing mining-induced damage (Burtan, 2017; Antonielli et al., 2021).

Primarily to ensure the safety of miners, but also to prevent or minimise mining damage, mining plants conduct research aimed at detecting emerging processes triggered by their operation, and implement relevant measures to reduce the extent of potential damage to underground and surface land structure. The basic scope of such research encompasses seismological monitoring and geodesic measurements of deformations. Currently, in order to improve the reliability of determinations, investigations on effects of mining operations on land include: shock monitoring systems, integrating all used measuring systems and software dedicated to processing monitoring data, to analyse ongoing changes in quasi-real time so that rapid response rescue services can be alerted in the event of exceeding safe values (Dawidowicz et al., 2021).

Seismometers, which detect vibrations of the Earth's crust triggered by its tremors and which record these parameters as displacements, velocities, and accelerations, are fundamental to the research of the Earth's surface tremors. Earthquake monitoring systems can be improved by coupling them with the Global Navigation Satellite System (GNSS). Based on satellite observations and ground-based support systems, the system facilitates accurate determination of point coordinates in a uniform 3D coordinate system. Data from inertial sensors for measuring displacements, specifically Inertial Measurement Units (IMUs), are often integrated with observational data from the GNSS, enabling the tracking of an object's movement in moments when satellite signals are lost (Paszek, 2016). Seismic wave detection using a single GNSS receiver, with an accuracy of a few centimeters, can also be achieved using a variometric approach (Colosimo et al., 2011). An example of a practical variometric application is the Leica Velocity and Displacement Autonomous Solution Engine (VADASE) solution (Leica Geosystems, 2015).

Because of their importance, shock monitoring systems need to be verified for the reliability of all detectors, for example, using devices designed to evaluate the strength of buildings exposed to earthquakes, such as the so-called shake tables, which generate vibrations of a specific direction, amplitude, and frequency. To evaluate the accuracy and reliability of measuring systems and devices that use GNSS and Inertial Navigation Systems (INSs) technologies for shock monitoring, a custom-built device was developed which simulates the occurrence of dynamic displacements reflecting actual frequencies and amplitudes expected over Polish territory. The device generating reciprocating motion by converting the rotary motion of a stepper motor is a dependable and low-cost alternative to shake tables, such as Quanser I-40 (Riley, 2017; Zheng et al., 2018).

2 Motivation for the development of a shake table

The purpose of the GNSS antenna vibration simulator is to assess the reliability and accuracy of measurement systems based on GNSS and INS technologies monitoring seismic shocks as well as other vibrations, for example, those detected during structural monitoring (Structural Health Monitoring, SHM), based on reciprocating motion with specific parameters. The GNSS antenna vibration simulator generates the movement of two satellite antennas of a specific amplitude, frequency, and direction. The reciprocating motion is generated through the transformation of the rotary movement of a stepper motor, the parameters of which can be set as required. The main purpose of the GNSS antenna vibration simulator is to collect high-frequency satellite data to assess the accuracy and reliability of computational programs that process satellite and inertial data and recording devices employed in seismographic systems.

Currently, GNSS satellite measurements are used routinely in terrain deformation studies. Static measurements, which allow the attainment of the accuracy of point coordinates up to a few millimetres, are typically employed in periodically conducted surveying task. In turn, the monitoring of displacement of points is most often supported by kinetic measurements made according to the Real-Time Kinematic (RTK)/Real-Time Network (RTN) methods, which determine of coordinates at an accuracy of single millimeters and frequency of 1 Hz. It would be beneficial in monitoring terrain deformations to acquire continuous information about the monitored points at an accuracy of single millimeters and the frequency of at least 20 Hz, which would allow for the detection of motions caused by earth tremors due to anthropogenic and natural forces. To determine these parameters at the required accuracy and reliability, adequate equipment for recording satellite data at a frequency of 50–100 Hz as well as appropriate measurement and processing procedures are needed. Essential data to be entered into the processing algorithms include information on the proper functioning of satellite systems and the atmospheric conditions (models of the ionosphere and troposphere-induced delays). Results in the form of point coordinates determined at the required accuracy can be obtained by selecting an appropriate calculation procedure which integrates the relevant elements. Verification of the accuracy and reliability of the results obtained from the carefully chosen calculation procedures should be preceded by practical verification consisting in inducing vibrations of the measurement point (GNSS antennas, an accelerometer) with specific, predefined motion parameters.

Vibration generators, commonly used in the construction industry for assessing the strength of structures in an environment emitting seismic vibrations, can be used for this purpose, as, used in laboratory conditions, they most often generate fading vibrations whose parameters are determined by motion detectors (accelerometers). Because of their substantial structural complexity and extensive control systems, these devices lack mobility, which is an important consideration in the calibration of seismic monitoring systems. To address the limitations of the existing vibration generating devices, the so-called shake tables, a GNSS antenna vibration simulator has been developed (Baryła et al., 2023), which can be used in field conditions.

A portable, low-cost 1D shake table designed for simulating land deformations (Figure 1) consists of a frame (1) with a motion guide (2) on which two trolleys (3 and 4) equipped with GNSS antennas (5 and 6) travel, and a stepper motor (7) fitted to the frame with an eccentric wheel (8) having an adjustable radius of the point of connection to a driving tie (9) attached to a trolley (3), to which ends of a driving cord (10) are connected. At both ends of the frame, driving rolls (11 and 12) are used to tense the driving cord, to which the second trolley (4) is attached. This configuration ensures that both trolleys move in opposite directions simultaneously during sliding motion. The stepper motor is coupled with a microprocessor control system (13). This construction allows for generation of correlated harmonic motion of two GNSS antennas, or other devices, e.g., accelerometers, with the set amplitude and frequency. The high-frequency readings made by GNSS receivers and other sensors, e.g., accelerometers, are then used to reproduce the parameters of the motion of the devices, such as amplitudes and frequencies from an analysis of time series, and to compare them with reference values (benchmark parameters) set in a simulation scenario.

The GNSS antenna vibration simulator is designed to continuously generate controlled vibrations with predefined amplitude, frequency, and direction. This is achieved through the use of a stepper motor coupled with a microprocessor-based controller, ensuring precise and repeatable motion patterns. A

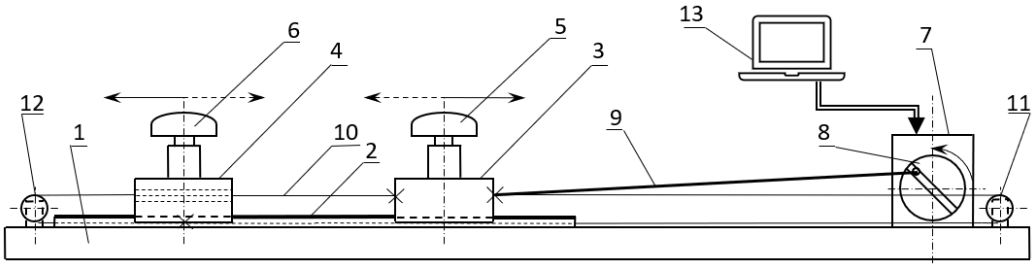

Figure 1. Schematic diagram of the structure of a vibration simulator

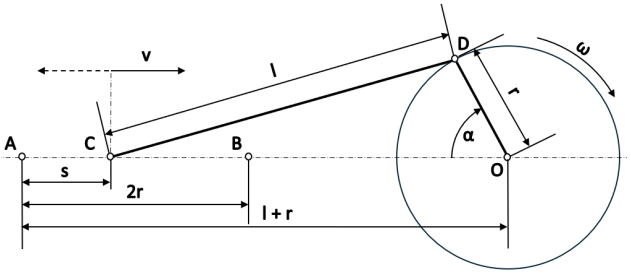

Figure 2. Diagram of a crank mechanism

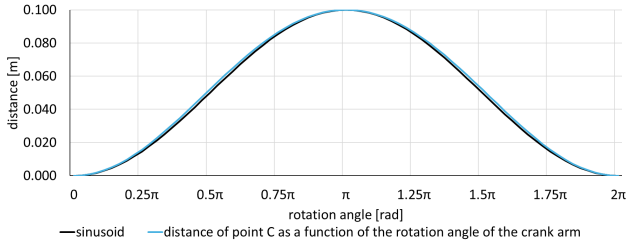

Figure 3. Graph of point C distance as a function of the rotation angle of the crank arm

second trolley with a GNSS antenna makes it possible to obtain additional, correlated kinematic observations, in addition to which, by inducing motion in the opposite direction to the first trolley, it compensates for moments of inertia caused by reciprocating motion, thus almost eliminating the device's own vibrations whilst working.

3 Analysis of reciprocating motion generated by a crank system

The displacement of a particle in periodic motion (a motion repeating in equal intervals of time) can be expressed by harmonic functions, sine, or cosine. A harmonic motion is an ordinary form of motion of observed physical phenomena.

The simplest mechanism demonstrating the relationship between reciprocating motion and rotary motion is a crank system commonly used in internal combustion engines. The diagram in Figure 2 shows a crank system composed of a crank arm OD of length r and a connecting rod CD of length l. The rotary motion of the crank rod with angular velocity ω around point O causes the motion of point D on a circle of radius r. Points A and B indicate the extreme positions of point C at values of the angle of rotation α equal 0 and π, respectively. The length of segment AB is equal to the double length of radius r, while the maximum distance reachable by point C at point A is $l + r$. Distance s travelled by point C depends on angle α and length of the connecting rod arm r (Kluczyk, 2014; Ikpe, 2020):

$$s = r\left(1 + \frac{k\sin^2\alpha}{2} - \cos\alpha\right), \tag{1}$$

where: k – ratio of the crank arm length to connecting rod length ($k = r/l$).

Velocity v of point C is the derivative of the distance with respect to time:

$$v = \frac{\mathrm{d}s}{\mathrm{d}t} = \frac{\mathrm{d}s}{\mathrm{d}\alpha}\cdot\frac{\mathrm{d}\alpha}{\mathrm{d}t} = r\left(\sin\alpha + \frac{k\sin 2\alpha}{2}\right)\frac{\mathrm{d}\alpha}{\mathrm{d}t}, \tag{2}$$

assuming that the derivative of the angle of rotation with respect to time is equal to the angular velocity, which can also be expressed using frequency f:

$$\frac{\mathrm{d}\alpha}{\mathrm{d}t} = \omega = 2\pi f. \tag{3}$$

And finally, the formula for the velocity of point C is as follows:

$$v = r\omega\left(\sin\alpha + \frac{k\sin 2\alpha}{2}\right). \tag{4}$$

The acceleration of the motion of point C is the derivative of velocity with respect to time, hence:

$$a = \frac{\mathrm{d}v}{\mathrm{d}t} = r\omega^2(\cos\alpha + k\cos 2\alpha). \tag{5}$$

An analysis of the variation of the above phenomena with respect to the reciprocating motion of point C as a function of the angle of rotation of the crank arm can be based on the comparison of the real functions with the plotted sine wave diagram visualising the motion of point C with the connecting rod parallel to the main direction. For the analysis of motion parameters, the following values were adopted: $r = 0.0500\,\mathrm{m}$, $l = 0.6000\,\mathrm{m}$, $f = 4\,\mathrm{Hz}$, $\alpha \in <0, 2\pi>$.

Using function (1), a graph of point C distance function (Figure 3), and a sine wave shifted in phase by 0.5π and with the amplitude equal the length of the crank arm r was plotted.

While analysing the variation of point C distance increments (Figure 3) with respect to the sinusoid, it emerges that the distance of point C converges with the sinusoid near extreme points A and B. In the remaining range, the length increments were greater than reference values, reaching the maximum values in the vicinity of the angles of the crank arm rotation of 0.5π and 1.5π; the distribution of the distance increments is symmetrical in reciprocating motion.

Based on function (4), a graph was plotted showing the velocity of point C as a function of the angle of rotation of the crank arm (Figure 4). The maximum values of the velocity equal 0.0210 m/s were obtained in the vicinity of angles 0.5π and 1.5π, at the extreme positions of point C at points A and B,

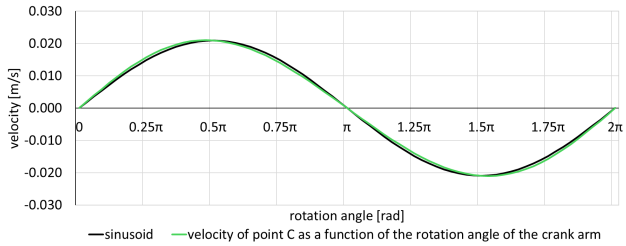

Figure 4. Graph of the velocity of point C as a function of the rotation angle of the crank arm

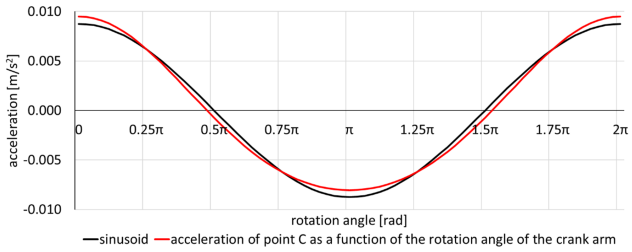

Figure 5. Graph of the acceleration of point C as a function of the rotation angle of the crank arm

where harmonic motion reverses the velocity vector's direction; for angles 0 (2π) and π, the value of the velocity equals zero. When comparing the function of velocity with the sinusoid of the amplitude of maximum velocity value $v_{max} = 0.0210$ m/s, four phases in reciprocating motion can be discerned: In the first and fourth phase for $\alpha \in (0, 0.5\pi) \wedge (1.5\pi, 2\pi)$, the increment in the velocity was greater than the reference values. Meanwhile, the increment in the velocity was lower than the reference values in the second and third phases for $\alpha \in (0.5\pi, \pi) \wedge (\pi, 1.5\pi)$. Additionally, in extreme points, the velocity function was shifted in the phase by approximately 5° towards extreme point A (Figure 2) – the maximum location of point C relative to the centre of rotation O.

Using function (5), the course of the point C acceleration function was plotted (Figure 5). Extreme acceleration values were observed near extreme points A and B, where the motion vector reverses. The maximum acceleration value of 0.0095 m/s^2 was reached at point A $(0, 2\pi)$ and the next extreme value of the function of -0.0080 m/s^2 was recorded at point B (π). The difference between the absolute values of acceleration in these extreme points follows from the characteristics of a crank system. To analyse the variation of the course of the acceleration function, a sinusoid with a phase shift of 0.5π and with an amplitude equal to the mean value of the absolute acceleration values in the extreme positions of point C, i.e., 0.0088 m/s^2, was adopted. In the analysis of the acceleration graph symmetric with respect to the angle of rotation π (Figure 5), two ranges can be distinguished, $\alpha \in (0.25\pi, 0.75\pi) \wedge (1.25\pi, 1.75\pi)$, in which the acceleration is lower than the reference values. At points where velocity peaks (Figure 4), the acceleration equals zero, and the null places of the displacement function are also phase-shifted by around 5° towards extreme point A.

Figure 6 illustrates results of a detailed comparison of the variations of the distance (Figure 3), velocity (Figure 4), and acceleration (Figure 5) functions of point C relative to the reference values. The distribution of the variation of the above increments is reflected by compressed sinusoids with periods π corresponding to single passes of point C. The blue colour indicates increments ds to the distance, which assume zero values in initial positions 0 and π and 2π, while the maximum differences in the distance increments occur for the rotation angles 0.5π and 1.5π (middle of reciprocating motion), achieving the

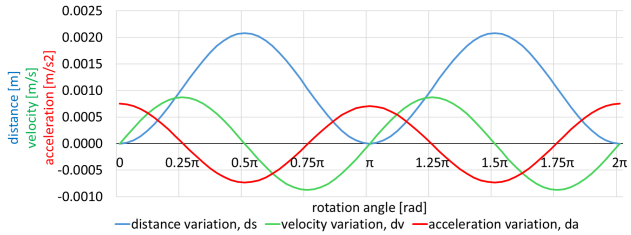

Figure 6. Changes in the parameters of the motion of point C, distance, velocity, and acceleration relative to the reference values

value equal to the double amplitude $ds_{max} = 0.0021$ m, which corresponds to 1.2% of the pass range ($2r = 0.1000$ m). The plotted graphs of velocity (green colour) and acceleration (red colour) increments are phase-shifted relative to the distance variation graph by -0.25π, -0.5π, respectively. The velocity variation function during one pass reaches three zero places for angles $0, 0.5\pi$ and π, and two extreme values for 0.25π, $dv_{max} = 0.0009$ m/s and 0.75π, $dv_{min} = -0.0009$ m/s. The amplitude in the graph showing the velocity variation function corresponds to 4.3% of the maximum value obtained for the velocity of point C. The acceleration variation function during one pass reaches two zero places for angles 0.25π and 0.75π, and three extreme values in extreme positions of point C for angles 0 and π, $da_{max} = 0.0008$ m/s^2 and 0.5π, $dv_{min} = -0.0008$ m/s^2. The amplitude in the graph of the velocity variation function corresponds to 8.4% of the maximum value of the acceleration recorded for point C.

An analysis of the percentages of the obtained increments relative to the determined reciprocating motion parameters using the crank system, determined based on the motion parameters adopted for the study shows that the variation of the distance can be studied according to the sinusoid. In contrast, investigations of the velocity and acceleration variation should consider functions (4) and (5), which significantly diverge from the reference values depicted by the sinusoid.

4 Experimental validation

An experiment was designed to explore the possibilities of using the in-house designed vibration simulator to validate the GNSS+IMU software and receivers dedicated to the detection of dynamic displacements. High-frequency GNSS data recorded in actual field conditions on the premises of the KGHM Cuprum CBR in Lubin, Poland, were used. Conducting the experiment in that location enabled us to leverage the nearby GNSS reference stations and record data under authentic field conditions.

Following the assumptions of the experiment, dynamic displacements were simulated by the developed vibration simulator (Figure 7). The simulation of harmonic motion in the east-west direction with an amplitude of 15.1 mm and frequency of 0.88 Hz was conducted. The dynamic motion of the GNSS antenna and receiver lasted 4 minutes, preceded by an initial one-minute static measurement, run to determine the initial position.

A low-cost GNSS receiver integrating a GNSS Septentrio Mosaic X5 module and a low-cost ADIS accelerometer as well as a Trimble Zephyr Geodetic 3 antenna were used to record the GNSS+IMU observations. In addition, the GNSS observations from the same antenna were recorded through a signal splitter with a professional, geodetic-grade Javad Alpha receiver, to compare the readings. Four nearby reference stations, between 3 and 7 km away, denoted as REF1, REF2, REF3 and REF 4, were equipped with Trimble Alloy receivers and TRM159900.00 an-

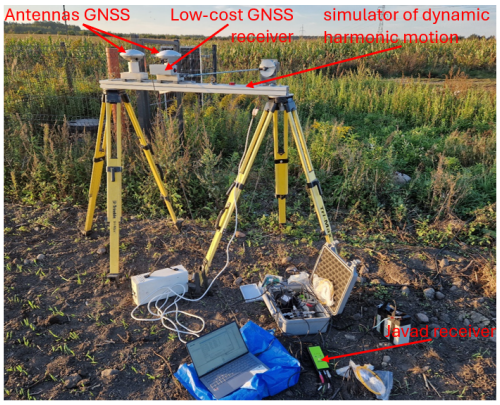

Figure 7. Simulator of dynamic displacements (harmonic motion) and low-cost GNSS receiver and Javad Alpha receivers during the measurement experiment in the study area

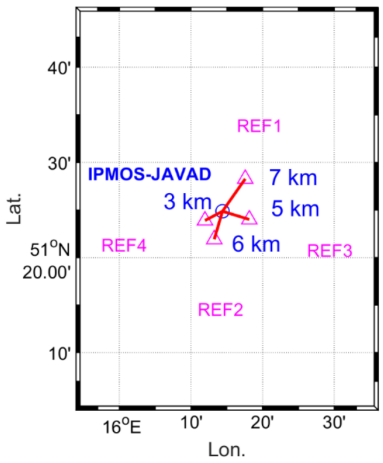

Figure 8. Location of mobile receivers (low-cost GNSS receiver and professional Javad) on a dynamic displacement simulator relative to the reference stations REF1, 2, 3, 4 in the study field

tennas. The GNSS observations were recorded by the two mobile receivers and the receivers at the reference stations at a frequency of 20 Hz. Accelerations from the IMU sensor were recorded at a frequency of 200 Hz by a built-in ADIS accelerometer in the GNSS receiver.

5 Processing of the GNSS data

The processing of GNSS observations consisted of four steps: import and preprocessing of input data, estimation of the parameters of the GNSS relative positioning model, integration of the GNSS and IMU solutions, and visualisation of the results. Having imported the observations, a solution based on GNSS observations was implemented, resulting in a time series of displacements in the local topocentric coordinate system. The kinematic determination of the position of the GNSS antenna was achieved using the readings from the four reference stations REF1, REF2, REF3 and REF4, located within the perimeter of the study field. Lengths of the vectors connecting the receivers calculated and the reference ones ranged from 3 to 7 km (Figure 8). By using GNSS observations with the recording frequency of 20 HZ, it was possible to obtain a kinematic solution of the position with the same interval.

Table 1. Noise of time series of displacements determined for the period without simulated displacements. Time series of coordinates unfiltered.

	low-cost GNSS receiver	Javad
STD_N [mm]	2.1	2.3
STD_E [mm]	1.1	1.7
STD_U [mm]	4.4	4.4

Table 2. Noise of time series of displacements determined for the period without simulated displacements. Time series of coordinates after filtration of low-frequency effects

	low-cost GNSS receiver	Javad
STD_N [mm]	1.1	1.4
STD_E [mm]	0.8	1.0
STD_U [mm]	1.6	2.2

6 Analysis of the noise of displacements time series derived from GNSS observations

The initial period of the GNSS high-frequency solution lasting 1 minute served to determine the initial coordinates and to make a preliminary analysis of the accuracy of the position determination by identifying the short-term noise of the displacement time series. The standard deviation of the three component displacement parameters was calculated, assuming that a change in the coordinates over the time when the antenna was immobile was an error in determining each component. The calculations were made for the time series of the original/raw coordinates and after low-frequency trends had been removed from these values.

Tables 1 and 2 show that for both the data filtered for low-frequency effects and the original positions, the solution obtained on the basis of observations from the low-cost GNSS receiver is characterised by lower noise as compared to the one obtained using the data from the Javad Alpha receiver. For the analysed period, the standard deviations of the original time series were in the range of 1–4 mm, depending on the component. Having removed the low-frequency trend from the time series, the standard deviation values decrease even below 2 mm for each of the components.

Figure 9 summarizes time series of displacements of the GNSS antenna determined based on the processed GNSS observations collected by the low-cost GNSS receiver and by a geodetic Javad Alpha receiver. The central panels show displacements in the east-west direction, in which the harmonic motion of the antenna was simulated. The diagrams enable us to read the response to the occurrence of harmonic motion one minute after the recording started in time series of displacements determined from both receivers.

7 Concordance assessment of the GNSS solutions: processing of the observations from low-cost GNSS receiver versus Javad Alpha receivers

In the next step in this study, the differences in displacements from the GNSS solutions obtained from the low-cost and Javad receivers throughout the whole data recording period of 5 minutes were calculated to establish their standard deviations. The standard deviation for the differences in displacements deter-

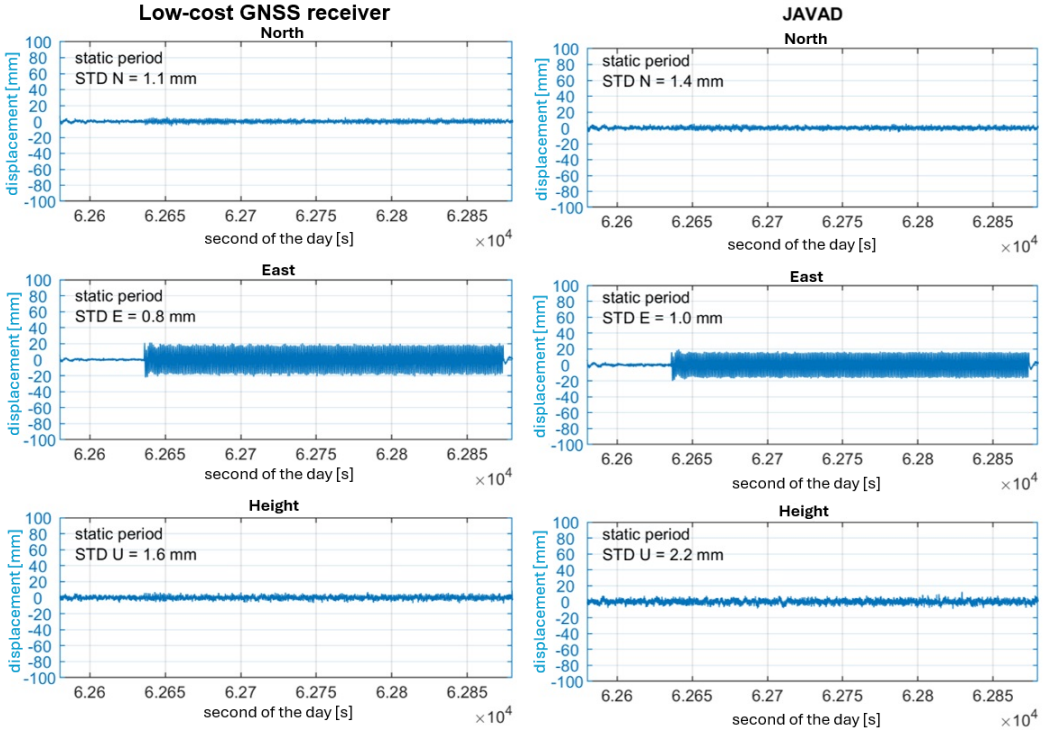

Figure 9. Time series of displacements obtained from the GNSS solution based on the observations captured by the Javad and by the low-cost GNSS receivers

mined according to the solutions based on the low-cost GNSS and Javad receivers were: STD_N = 1.3 mm, STD = 2.0 mm, STD_U = 2.2 mm. These values document high concordance between determinations of coordinates obtained from processing the observations collected by the low-cost receiver and the professional Javad Alpha receiver.

Figure 10 shows a close-up of a sample period of 10 s from a time series of displacements obtained from a 20 Hz GNSS solution based on the data collected by the low-cost and Javad Alpha receivers. The subsequent panels of the diagram illustrate the high coincidence of the two GNSS solutions for its equivalent components. Of particular significance is the high coincidence of displacements obtained for the eastern components, in which the dynamic motion of the antenna was simulated.

Considering the above results, the following conclusions can be drawn:

- Remarkably high concordance was achieved between high-frequency determinations of displacements for the GNSS data collected by the Javad Alpha receiver and the low-cost receiver.
- It is possible to obtain short-term time periods of displacements with a high-frequency solution (20 Hz) and observational noise of approximately 2 mm for each of the three displacement components.

8 The processing and analysis of the GNSS+IMU integrated solution

The final high-frequency solution applied to detect dynamic displacements was based on the integration of the GNSS technology and accelerations recorded by an IMU sensor. This analysis constituted the third step of this study. Figure 11 compares the obtained time series of displacements and accelerations recorded by the low-cost GNSS receiver for the whole period of the harmonic motion excitation. The red colour shows the final integration of the GNSS+IMU (accelerometer) solution

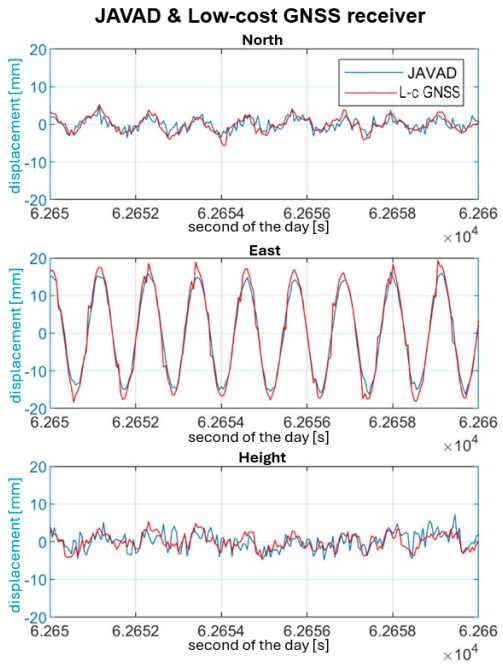

Figure 10. Comparison of time series of displacements from the GNSS solutions based on observations collected by the Javad and low-cost GNSS receivers. A close-up on a 10-second time window.

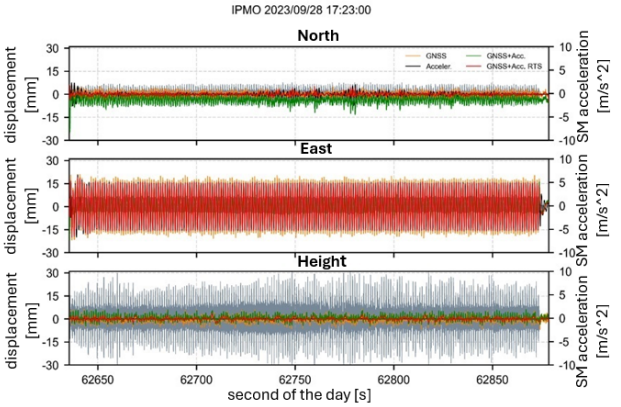

Figure 11. Time series of displacements obtained from the GNSS+IMU (accelerometer) integrated solution – green, GNSS+IMU (accelerometer) smoothed with the RTS algorithm – red, GNSS-only – orange, IMU-only (accelerometer) – black, based on observations collected by the low-cost GNSS receiver. The grey colour in the background illustrates the accelerations recorded by the IMU accelerometer.

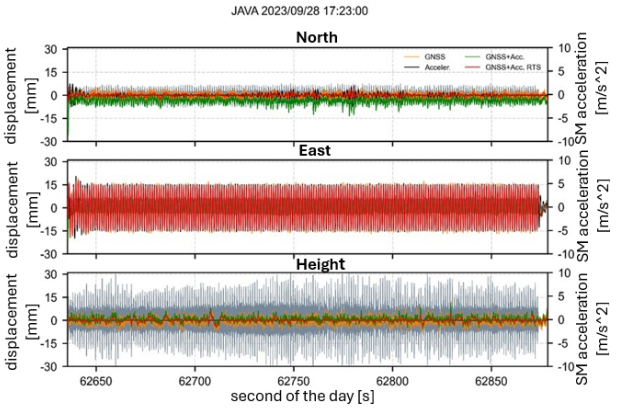

Figure 12. Time series of displacements obtained from the GNSS+IMU (accelerometer) integrated solution – green colour, GNSS+IMU (accelerometer) smoothed with the RTS algorithm – red, GNSS-only – orange, IMU-only (accelerometer) – black, based on observations collected by the Javad receiver. The grey colour in the background illustrates the accelerations recorded by the IMU accelerometer.

smoothed with the Rauch Tung Striebel (RTS) algorithm. The intermediate solutions, i.e., the integrated GNSS+IMU, GNSS-only, and IMU-only, are indicated by colours: green, orange, and black, respectively. Figure 12 shows the corresponding values, but achieved from the solution based on GNSS data collected by the professional JAVAD Alpha receiver. Figures 13 and 13 illustrate a time series of displacements from the final GNSS+IMU RTS solutions conducted with the use of the low-cost GNSS receiver and Javad Alpha receivers. The plotted graphs demonstrate that the in-house developed GNSS+IMU module applied to the processing and integration of observations renders reliable reproduction of responses (displacements) to the simulated harmonic motion. Figure 15 compares the time series of displacements from the final integrated GNSS+IMU RTS solution based on the data recorded by the low-cost receiver and the professional Javad Alpha receiver, characterised by high coincidence.

A Fourier transform-based analysis was applied to a time series of displacements obtained from the HR GNSS+IMU obser-

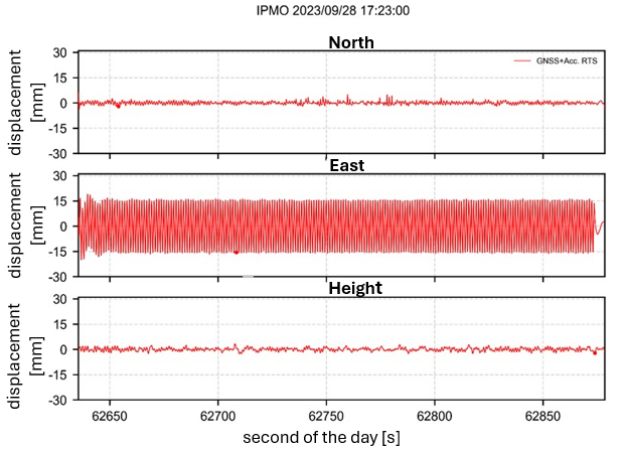

Figure 13. Time series of displacements obtained from the GNSS+IMU integrated solution smoothed with the RTS algorithm, based on the processed observations collected by the low-cost GNSS receiver

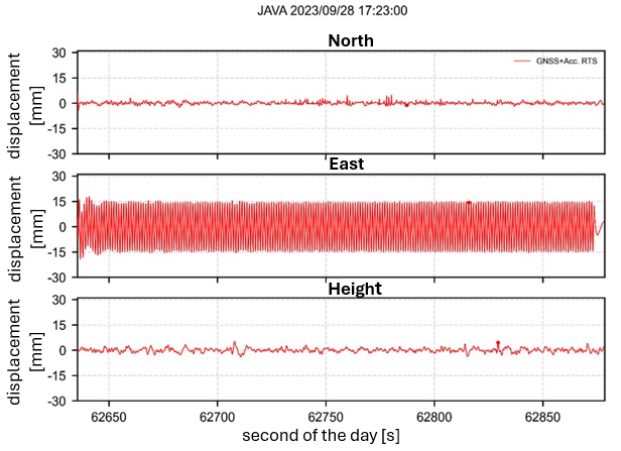

Figure 14. Time series of displacements obtained from the GNSS+IMU integrated solution smoothed with the RTS algorithm, based on the processed observations collected by the Javad receiver and IMU observations from the low-cost receiver

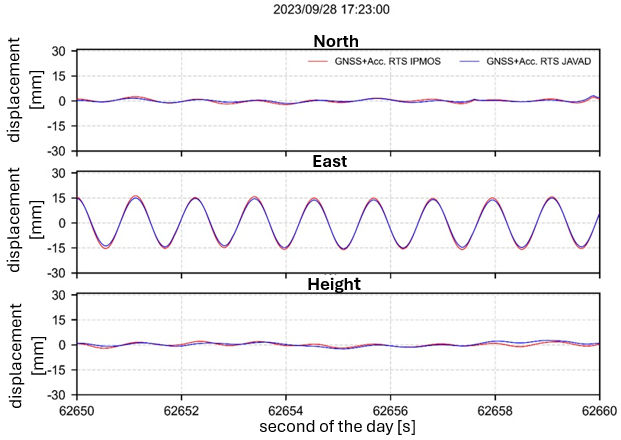

Figure 15. A close-up on a 10-second period series of displacements from integrated solutions GNSS+Acc. (IMU accelerometer) smoothed with the RTS algorithm based on GNSS observations collected by the Javad receiver and the low-cost receiver and IMU observations recorded by the low-cost receiver

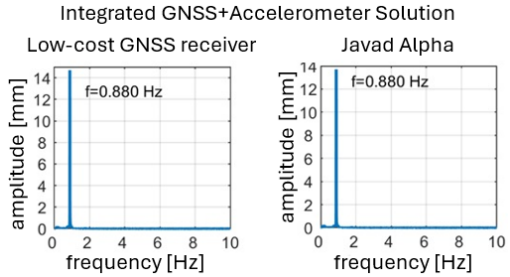

Figure 16. Results of a Fourier transform-based analysis (amplitude spectrum) of time series of displacements obtained from GNSS+IMU RTS integrated solutions based on GNSS observations collected by the Javad and low-cost GNSS receiver and IMU observations recorded by an ADIS accelerometer

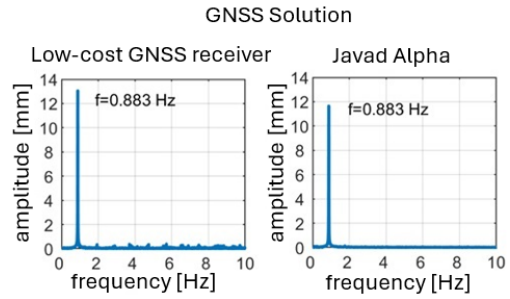

Figure 17. Results of a Fourier transform-based analysis (amplitude spectrum) of time series of displacements obtained from GNSS observations collected by the Javad and low-cost GNSS receiver

vation processing module and observations from the low-cost GNSS receiver. The purpose of the analysis was to reproduce the frequency and amplitude from the time series of displacements, and to compare these values to the set parameters of the harmonic motion excited by the in-house developed vibration simulator. Based on the analysis, the accuracy of the determination of dynamic displacements was assessed. The reference parameters of harmonic motion set in the experiment were: frequency f = 0.88 Hz, amplitude A = 15.1 mm. Figure 16 shows the FFT spectra for the final results obtained from the GNSS+IMU RTS integrated solution, while Figure 17 displays the same data but for the solution using only GNSS observations. Table 3 compares values of the determined parameters characterising the harmonic motion reproduced from the time series of the recorded displacements.

Results of the analysis of time series with the Fourier transform show high concordance of the dynamic displacements obtained from observations collected by the GNSS+accelerometer

Table 3. Values of amplitudes and frequences detected with the use of the Fourier transform (amplitude spectrum) from time series of displacements for the GNSS+IMU RTS integrated solution and the GNSS solution based on data collected by the low-cost GNSS receiver and Javad receivers and IMU observations recorded by the low-cost GNSS receiver

Reference parameters of simulated motion: A=15.1 mm, f=0.88 Hz	**Low-cost GNSS**		**Javad Alpha**	
	A [mm]	**f [Hz]**	**A [mm]**	**f [Hz]**
GNSS+Acc. RTS	14.7	0.8805	13.7	0.8805
GNSS	13.1	0.8833	11.6	0.8833

set and the set values simulated by the in-house developed device. Differences between detected amplitudes relative to the known amplitudes of the simulated harmonic motion were only 0.4 mm for the final integrated GNSS+IMU solution based on observations from the low-cost GNSS receiver. Moreover, the GNSS+IMU integrated solution has a significant advantage over the solution based only on GNSS observations, as the differences between the determined amplitude and the set one are higher for the GNSS solution, reaching values between 2.0 mm and 3.5 mm, depending on the employed GNSS receiver.

9 Conclusions

The occurrence of tremors on the Earth's surface, caused by natural or anthropogenic forces, can have an extremely negative impact on technical infrastructure and the safety of people present near the epicentre of an earthquake. This justifies the need for investigations of earthquakes and tremors with the use of new but widely available measurement instruments that supplement the data acquired using seismographs. Among such instruments are new-generation low-cost GNSS/GNSS+IMU receivers. As this technology is relatively new, it requires robust testing of its performance. An example of a tool suitable to evaluate low-cost receivers is the simulator of GNSS antenna vibrations presented in this paper. This is a device with a plain design and effortless operation, which generates parameters of harmonic motion described with adequate functions visualized by sinusoids. The device was evaluated in field conditions, by generating displacements with strictly specified parameters (amplitude, frequency), which should be recorded by the GNSS+IMU motion detectors employed for this purpose.

The results of the research obtained from the experiments indicate high correlation of the parameters of harmonic motion determined in the form of time series with the parameters generated by the vibration simulator, which confirms the usefulness of the tested device for validation of new measurement systems. The results of the analysis of displacement time series made with the Fourier transform show high concordance between the dynamic displacements obtained from the GNSS+IMU observations and the values generated by the in-house developed device. Differences of the detected amplitudes with respect to the known amplitude of the simulated harmonic motion did not exceed 0.4 mm. It is worth noting that while using the proposed device in the experiments, we were able to conduct satellite observations simultaneously with the tested low-cost GNSS receiver and the geodetic Javad Alpha receiver with the use of the same GNSS antenna. As another benefit from the this study the low-cost GNSS receivers were validated as rendering precise readings.

References

Antonielli, B., Sciortino, A., Scancella, S., Bozzano, F., and Mazzanti, P. (2021). Tracking Deformation Processes at the Legnica Glogow Copper District (Poland) by Satellite InSAR—I: Room and Pillar Mine District. *Land*, 10(6):653, doi:10.3390/land10060653.

Baryła, R., Paziewski, J., and Wielgosz, P. (2023). Prawo ochronne nr 72933 na wzór użytkowy pt.: Symulator drgań anten GNSS, zwłaszcza dla potrzeb wyznaczenia deformacji terenu (Protection right no. 72933 for the utility model entitled: GNSS antenna vibration simulator, especially for the purpose of determining terrain deformations). Technical report, The Patent Office of the Republic of Poland.

Burtan, Z. (2017). The influence of regional geological settings

on the seismic hazard level in copper mines in the Legnica-Głogów Copper Belt Area (Poland). *E3S Web of Conferences*, 24:01004, doi:10.1051/e3sconf/20172401004.

Colosimo, G., Crespi, M., and Mazzoni, A. (2011). Real-time GPS seismology with a stand-alone receiver: A preliminary feasibility demonstration: Real-Time GPS Seismology. *Journal of Geophysical Research: Solid Earth*, 116(B11302), doi:10.1029/2010jb007941.

Dawidowicz, K., Rapiński, J., Śmieja, M., Wielgosz, P., Kwaśniak, D., Jarmołowski, W., Grzegory, T., Tomaszewski, D., Janicka, J., Gołaszewski, P., Wolak, B., Baryła, R., Krzan, G., Stępniak, K., Florin-Catalin, G., and Brzostowski, K. (2021). Preliminary Results of an Astri/UWM EGNSS Receiver Antenna Calibration Facility. *Sensors*, 21(14):4639, doi:10.3390/s21144639.

Duff, D., Valley, B., Milkereit, B., and McGaughey, W. (2011). Rock mass response to deep mining induced stress—research and tools development at the CEMI, Canada. In *Proceedings of the Fourth International Seminar on Strategic versus Tactical Approaches in Mining*, Strategic versus Tactical 2011, pages 73–84. Australian Centre for Geomechanics, Perth, doi:10.36487/acg_rep/1108_07_duff.

Galos, K., Lewicka, E., and Smakowski, T. (2010). Podstawowe trendy zmian w gospodarowaniu surowcami mineralnymi w Polsce na przestrzeni ostatnich dwudziestu lat (Basic trends in the management of mineral resources in Poland over the last twenty years). *Zeszyty Naukowe Instytutu Gospodarki Surowcami Mineralnymi i Energią PAN*, (79):7–30.

Ikpe, A. (2020). Design Analysis of Reciprocating Piston for Single Cylinder Internal Combustion Engine. *International Journal of Automotive Science and Technology*, 4(2):30–39, doi:10.30939/ijastech..702219.

Kluczyk, M. (2014). An analysis of the kinematics and dynamics of a shaft-piston system in a single cylinder four-stroke engine ZS. *Scientific Journal of Polish Naval Academy*, 198(3), doi:10.5604/0860889x.1133254.

Leica Geosystems (2015). Leica VADASE Autonomously detecting fast movements in real time. https://leica-geosystems.com/-/media/files/leicageosystems/products/flyer/leica_vadase_fly.ashx?la=en.

Paszek, J. (2016). Analiza błędów losowych czujników bezwładnościowych przy pomocy metod wariancyjnych (Random error analysis of inertial sensors using variance methods). *Przegląd Elektrotechniczny*, 1(1):64–69, doi:10.15199/48.2016.01.14.

Riley, C. (2017). *Dynamic Evaluation of Transportation Structures with iPod-Based Data Acquisition*. National Institute for Transportation and Communities (NITC-ED-985), doi:10.15760/trec.166.

Sainoki, A., Maina, D., Schwartzkopff, A. K., Obara, Y., and Karakus, M. (2020). Impact of the intermediate stress component in a plastic potential function on rock mass stability around a sequentially excavated large underground cavity. *International Journal of Rock Mechanics and Mining Sciences*, 127:104223, doi:10.1016/j.ijrmms.2020.104223.

Shirani Faradonbeh, R., Taheri, A., and Karakus, M. (2022). The propensity of the over-stressed rock masses to different failure mechanisms based on a hybrid probabilistic approach. *Tunnelling and Underground Space Technology*, 119:104214, doi:10.1016/j.tust.2021.104214.

Szuflicki, M., Malon, A., and Tymiński, M. (2024). Bilans zasobów złóż kopalin w Polsce wg stanu na 31 XII 2023 r. (Balance of mineral resources in Poland as of December 31, 2023). Technical report, Państwowa Służba Geologiczna, Państwowy Instytut Geologiczny – Państwowy Instytut Badawczy.

Zheng, Y.-G., Huang, J.-W., Sun, Y.-H., and Sun, J.-Q. (2018). Building Vibration Control by Active Mass Damper With Delayed Acceleration Feedback: Multi-Objective Optimal Design and Experimental Validation. *Journal of Vibration and Acoustics*, 140(4), doi:10.1115/1.4038955.